ACS APPLIED MATERIALS & INTERFACES

www.acsami.org

Research Article

Integration of a Metal–Organic Framework Film with a Tubular Whispering-Gallery-Mode Microcavity for Effective CO_2 Sensing

Ye Kong, Zhe Zhao, Yunqi Wang, Shuo Yang, Gaoshan Huang,* Yang Wang, Chang Liu, Chunyu You, Ji Tan, Chao Wang, Borui Xu, Jizhai Cui, Xuanyong Liu, and Yongfeng Mei*

Cite This: *ACS Appl. Mater. Interfaces* 2021, 13, 58104–58113

Read Online

ACCESS | Metrics & More | Article Recommendations | Supporting Information

ABSTRACT: Carbon dioxide (CO_2) sensing using an optical technique is of great importance in the environment and industrial emission monitoring. However, limited by the poor specific adsorption of gas molecules as well as insufficient coupling efficiency, there is still a long way to go toward realizing a highly sensitive optical CO_2 gas sensor. Herein, by combining the advantages of a whispering-gallery-mode microcavity and a metal–organic framework (MOF) film, a porous functional microcavity (PF-MC) was fabricated with the assistance of the atomic layer deposition technique and was applied to CO_2 sensing. In this functional composite, the rolled-up microcavity provides the ability to tune the propagation of light waves and the electromagnetic coupling with the surroundings via an evanescent field, while the nanoporous MOF film contributes to the specific adsorption of CO_2. The composite demonstrates a high sensitivity of 188 nm RIU^{-1} (7.4 pm/% with respect to the CO_2 concentration) and a low detection limit of ~5.85×10^{-5} RIU. Furthermore, the PF-MC exhibits great selectivity to CO_2 and outstanding reproducibility, which is promising for the next-generation optical gas sensing devices.

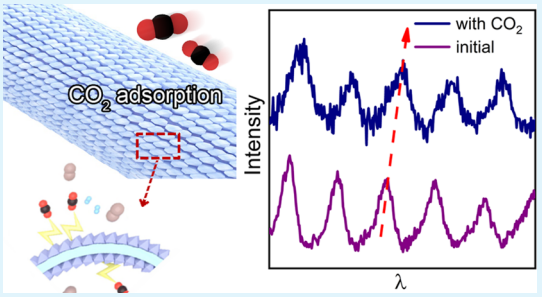

KEYWORDS: *optical microcavity, metal–organic framework, nanoporous, carbon dioxide sensor, evanescent coupling*

1. INTRODUCTION

Nowadays, the CO_2 concentration in the atmosphere is continuously increasing, thus the measurement and control of CO_2 emissions are becoming more and more important.[1,2] CO_2 measurements are required in the agriculture industry,[3] biochemical process management,[4] and industrial emission monitoring.[5] Especially, in the field of industrial combustion, which is the main source of CO_2 emissions, the CO_2 content of the exhaust gas will reach 10 to 20%.[6] For instance, in boiler feed water heaters, the CO_2 content of the emitted flue gas will reach more than 80%.[7] Thus, high-performance CO_2 sensors that can quantitatively sense CO_2 with low power consumption and a wide working range are attracting tremendous attention.[8,9] To date, the most common types of CO_2 sensors available are infrared (IR)-based[10] and semiconductor-based conductometric gas sensors.[11,12] Non-dispersive IR-based gas sensors have the characteristics of fast response, non-toxicity, great durability, and so forth, and they have been widely used for the most common needs.[10] The recently developed surface-enhanced IR adsorption (SEIRA) spectroscopy also serves as an effective method on a nanoscale for the detection of sparsely dispersed gas molecules.[13] However, IR-based sensors which need a specific IR source are normally relatively big with larger power consumption, which hinders their use in on-chip applications.[10] On the other hand, application of semiconductor-based sensors is limited due to their high operating temperature (over 100 °C),[14] low sensitivity,[15] and poor selectivity.[16] In addition, the working range of these sensors is generally inadequate for industrial applications.[6]

Optical sensors based on refractive index (RI) change have become an alternative gas detection tool owing to their handheld capability and room-temperature operation.[17−19] As promising candidates, optical fiber-based sensors[20,21] and whispering-gallery-mode (WGM) microcavity-based sensors[22] were developed and applied in sensing the surrounding environment.[23−27] Specifically, the WGM microcavity is a resonator that can confine light through resonance.[28−32] The change of the RI of the surrounding medium influences resonance in the microcavity via the intermediate effect of the evanescent field,[33] and the corresponding shift of the resonant wavelength is engaged as a probe to sense the environmental change. Especially, in the case of rolled-up microtubes, the microring-like cross section also acts as a WGM resonator,[33,34] while the subwavelength tube wall leads to an intensified evanescent field in the surrounding environment,[31] and the

Received: August 25, 2021
Accepted: November 11, 2021
Published: November 23, 2021

https://doi.org/10.1021/acsami.1c16322
ACS Appl. Mater. Interfaces 2021, 13, 58104–58113

enhanced coupling from the evanescent field greatly promotes the sensitivity in a large working range.[25,26,33,34] The wide spectral range and the tubular geometry make it an ideal candidate for on-chip sensing devices, especially in an optofluidic system for real-time sensing of a tiny amount of sample.[34] However, application of pristine WGM microcavities in sensing highly sparse media such as gases is still challenging due to their poor gas adsorption with low selectivity.[35] The small amount of target gas molecules in the nearby region causes a negligible RI change, and the corresponding weak coupling can hardly lead to detectable variation of the evanescent field. This suggests that the rolled-up WGM microcavity may not be suitable for gas sensing. In order to enhance the coupling between the gas molecules and the evanescent field, we consider that collecting the gas molecules in the region close to the resonator wall should be an effective option to enhance the coupling. Modification of the surface of the resonator by using functional materials with specific gas adsorption ability is therefore of importance from the viewpoints of both fundamental and practical research.

To modify a microcavity to achieve CO_2 sensing from enhanced evanescent coupling, we introduced a metal−organic framework (MOF) film into the microtubular cavity. MOFs are a series of porous materials consisting of metal ions with organic bridging ligands.[36] Due to the large specific surface area,[37] large and abundant pore volume,[38] and stable structure,[39] MOFs have been widely used in gas adsorption and separation.[37,39,40] Zeolitic imidazolate framework-8 (ZIF-8) is an important subclass among MOFs,[41] and it can effectively absorb CO_2 molecules since the slit width of the pores in ZIF-8 is similar to the dynamic diameter of CO_2 molecules (about 3.4 Å).[20,42] The quadrupolar interaction between carbon and nitrogen atoms of the ZIF-8 structure also promotes the adsorption rate.[43,44] Previously, Lee et al.[13] achieved sensing of CO_2 through the combination of ZIF-8 and SEIRA. We consider that the surface modification of the WGM microcavity with ZIF-8 should also lead to effective gathering of CO_2 molecules to produce a stronger coupling, and consequently a high sensitivity could be expected. It is worth noting that, compared with other modification layers (e.g., polyethylenimine) which concentrates certain gas molecules,[45,46] the diversity of MOF-related materials might make the MOF-modified WGM microcavity capable of detecting various gases.

So far, approaches to integrate MOFs with certain substrates are quite limited, and weak attachment and non-uniformity due to particle aggregation and irregular dispersion are noted.[47] Fabrication of uniform and smooth MOF films is crucial to the MOF-decorated WGM microcavity because the rough surface with remarkable light scattering should deteriorate the performance of the sensor.[48,49] Recently, an efficient strategy by utilizing an oxide nanomembrane prepared by atomic layer deposition (ALD) to induce the growth of a uniform MOF film on complex substrates was developed.[36,50,51] The firm adhesion between the functional layer and the substrate endows the composites with excellent structural stability for practical applications.[36,50,52,53]

Herein, a "MOF−tube−MOF" structure, where a rolled-up WGM microcavity was flanked by ZIF-8 films serving as modification layers, was realized by assembling ZIF-8 films on the tube wall via an ALD oxide induction layer and the following gaseous growth process. Theoretical calculations were carried out based on the finite element method (FEM), and experimental characterizations confirm that the so-called porous functional microcavity (PF-MC) can achieve highly sensitive CO_2 sensing due to the collection of CO_2 molecules in the ZIF-8 film. The sensitivity of the PF-MC is up to 188 nm RIU^{-1} with a low limit of detection (LOD) of $\sim 5.85 \times 10^{-5}$ RIU. Due to its outstanding structural stability, great sensing reproducibility is also achieved in terms of 50 stable repeated sensing and recovery cycles. The experimental results also demonstrate high selectivity and excellent anti-interference ability for the device, inheriting specific CO_2 adsorption for ZIF-8 films. This work provides a new approach for optical gas sensing with great potential for future applications. It is quite meaningful that the WGM microcavities actually serve as platforms and various MOF films can be applied as catchers for the corresponding gas molecules, thus an integrated multifunctional gas sensing system will be produced.

2. EXPERIMENTAL SECTION

2.1. Materials. 2-Methylimidazole (2-MI) was purchased from Aladdin Ltd. (Shanghai, China). All the reagents were used as received without further purification. The deionized water (DI water) used throughout all experiments was purified through a Millipore system.

2.2. Fabrication of Rolled-Up Microtubes. The structure in the current work is based on a silicon substrate from the cut and cleaned silicon wafer. First, a uniform ARP-3510 photoresist (Allresist GmbH) layer with a thickness of ~2 μm was spin-coated on the silicon substrate. The photoresist layer was then patterned to arrays of circles with various diameters by ultraviolet lithography (SUSS MA6) and used as the sacrificial layer. The pre-strained Y_2O_3/ZrO_2 bilayers with a thickness of 15/60 nm were deposited by electron beam deposition with a glancing angle of 30° at deposition rates of 5 and 0.5 Å s^{-1}, respectively. Acetone was applied to selectively remove the sacrificial layer and release the pre-strained oxide bilayer. The critical point dryer (Leica CPD 030) was employed to dry the rolled-up oxide microtubes with liquid CO_2.

2.3. Fabrication of an Oxide Nanomembrane as an Induction Layer. An Al_2O_3 nanomembrane was first deposited as an adhesion layer by the ALD technology. The deposition of the Al_2O_3 nanomembrane on the exposed surface of the microtubes was performed at 120 °C in a homemade reactor. Trimethylaluminum (TMA) and DI water were used as precursors. A typical ALD cycle included a TMA pulse (30 ms), waiting time (5 s), a N_2 purge (30 s), a DI water pulse (30 ms), waiting time (5 s), and a N_2 purge (30 s). In the current study, the Al_2O_3 nanomembrane was deposited on microtubes with 30 ALD cycles. A ZnO nanomembrane was then deposited at 150 °C. Diethylzinc (DEZ) and DI water were used as precursors. A typical ALD cycle included a DEZ pulse (30 ms), waiting time (5 s), a N_2 purge (30 s), a DI water pulse (30 ms), waiting time (5 s), and a N_2 purge (30 s). In the current study, the ZnO nanomembrane was deposited on microtubes with 50 ALD cycles.

2.4. Gas-Phase Synthesis of ZIF-8 Films on the Roll-Up Microcavity. 2-MI powder was ground with an agate mortar which served as a precursor to synthesize the ZIF-8 layer. The rolled-up microcavity array on the silicon wafer was attached to the porcelain boat with a polyimide tape and was combined with another porcelain boat containing 2-MI powder to form a sealed reaction chamber. The chamber was then put into a tube furnace and kept at 180 °C for 3 h in a N_2 atmosphere, during which time the ZnO induction layer reacted with 2-MI to form ZIF-8 films.

2.5. Structural and Compositional Characterizations. The morphologies of all the products were characterized by field emission scanning electron microscopy (FESEM) using a VEGA TS 5136 MM (TESCAN Co., Czech) system. The cross-sectional morphology was characterized by transmission electron microscopy (TEM) (JEM-2100F). X-ray diffraction (XRD) patterns were obtained by using an X'Pert Pro X-ray diffractometer equipped with Cu Kα radiation (λ =

https://doi.org/10.1021/acsami.1c16322
ACS Appl. Mater. Interfaces 2021, 13, 58104−58113

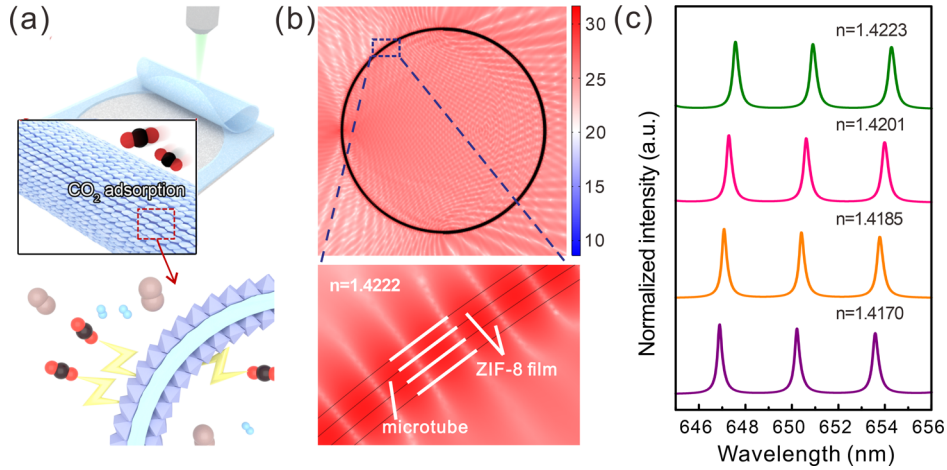

Figure 1. Schematic of the structure and the simulation of the sensing mechanism. (a) Schematic of the structure of PF-MC. The inner and outer surfaces are decorated by ZIF-8 layers for CO_2 adsorption. (b) Simulated distribution of the electric field in the case of resonance, and the blue dashed box is enlarged in the lower panel. The intensity of the electrical field is logarithmically processed. (c) Simulated spectra of PF-MC with ZIF-8 film's RI changed.

0.1542 nm) at a current of 40 mA and a voltage of 40 kV. In order to analyze the oxygen vacancies in the sample, electron spin resonance (ESR) spectroscopy was performed with the Bruker EMX PLUS, and the center field was set as 3510 G. A QUADRASORB adsorption instrument (Quantachrome Instruments) was used to perform the nitrogen sorption/desorption measurements. The specific surface area was calculated using the single-point Brunauer–Emmett–Teller (BET) method. The pore size distributions were calculated from the nitrogen sorption data using the nonlocal density functional theory equilibrium model method for slit pores provided by Quantachrome data reduction software ASiQwin version 4.01. An energy-dispersive spectrometer (Oxford XMax 80T) was utilized to analyze the composition of the sample. X-ray photoelectron spectroscopy (XPS) analyses were performed with a VG ESCALAB 220I-XL device. Curve fitting for all the XPS spectra was accomplished by using XPS Peak 4.1 software. Raman spectra were recorded on the HORIBA LabRAM HR Evolution under the excitation of a 532 nm laser.

2.6. Characterization of the Sensing Performance. The optical sensing performance of a device in different atmospheres was studied by a Raman spectrometer with an excitation wavelength of 532 nm (HORIBA LabRAM HR Evolution). The output laser power was adjusted to 2.5 mW. The sensor was placed in a testing chamber with a quartz window, and the flow rates of gases (e.g., CO_2, N_2, O_2, and H_2) flowing into the chamber were tuned and monitored by flowmeters. The total flow rate was maintained at 100 mL min^{-1} when the gas mixture was used. The change in CO_2 concentrations was realized by controlling the flow rates of CO_2 and N_2 and the ratio. The experiment was performed at room temperature.

2.7. Theoretical Model. Theoretical calculations were performed by the FEM, while the geometrical parameters were obtained from morphological characterizations. In the theoretical model, the Y_2O_3/ZrO_2 nanomembrane with a total thickness of 75 nm rolled 1.5 rotations to produce the rolled-up microtube with a diameter of 23 μm, while ZIF-8 films with thickness of 75 nm were coated on both the inner and outer surfaces of the microtube. The RI of the oxide tube wall was set as 1.8 for the e-beam evaporation-deposited Y_2O_3/ZrO_2 bilayer. The mesh size of the structure was set to be less than 1/3 of the wavelength to ensure the accuracy. The simulation was conducted in the electromagnetic wave frequency domain and the resonant wavelengths were obtained by calculating the eigenfrequencies of the structure (with perfect matched layers on the boundary).

3. RESULTS AND DISCUSSION

3.1. Theoretical Simulation of the MOF-Decorated WGM Microcavity. Figure 1a shows a schematic of the PF-MC for CO_2 sensing. The wall of the microtubular WGM cavity is sandwiched by two ZIF-8 films to form a "MOF–tube–MOF" structure. When the composite comes in contact with CO_2 molecules, the specific gas adsorption results in the gathering of CO_2 molecules in ZIF-8 layers, leading to amplified RI change and stronger coupling between molecules and the evanescent field. This effect should be visualized through the shift of the resonant wavelength. We then carried out theoretical simulation to verify this design. Here, the FEM is applied to calculate the shift of resonant wavelengths as a function of RI change.[54] Figure 1b shows a typical image of the distribution of the electrical field when resonance occurs, and the lower panel shows a partial enlargement. As shown in the enlarged image, the theoretical model consists of three layers, including the inner MOF film, the tube wall, and the outer MOF film. The distribution pattern of the electric field in the three layers can be clearly seen, and the evanescent field is obvious due to the subwavelength thickness of the three layers. Here, RI = 1.4170 is adopted in the calculation of ZIF-8 films without adsorption of CO_2.[55] With the increase of RI of the MOF layer due to CO_2 adsorption,[55] a red shift of the resonant wavelength in the spectra can be clearly observed, as demonstrated in Figure 1c. The calculation results therefore confirm the gas-sensing ability of the PF-MC.

3.2. Morphological and Compositional Analyses. Experimentally, a PF-MC was prepared by combining the rolled-up technology and ALD ZnO nanomembrane-induced gaseous growth of the ZIF-8 layer. The fabrication process is schematically shown on the top of Figure 2. Rolled-up microtubes were first prepared by releasing the pre-strained 75 nm Y_2O_3/ZrO_2 bilayer through the removal of the sacrificial layer.[33,54] The vertical strain gradient thus leads to the assembly of the oxide microtubular cavity.[28,30] With the help of photolithography, mass production of such microtubes can also be achieved (Figure S1).[33] The SEM images in Figure 2a,b with different magnifications demonstrate the array of Y_2O_3/ZrO_2 microtubes with a smooth surface. The ALD coating process was then employed to grow a uniform and thickness-controllable ~2.7 nm Al_2O_3 layer (adhesion layer) and a ~8.5 nm ZnO layer on the as-prepared bare microtube (ALD-ZnO–Y_2O_3/ZrO_2). As shown in Figures 2c,d, and S2, by performing the ALD coating on the bare microtubes, no

https://doi.org/10.1021/acsami.1c16322
ACS Appl. Mater. Interfaces 2021, 13, 58104–58113

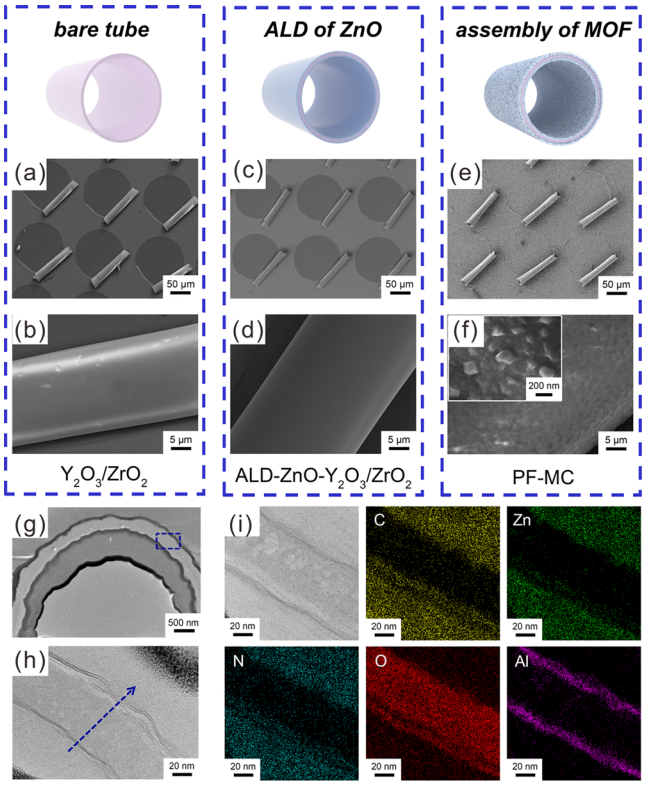

Figure 2. Morphological and compositional characterizations of samples. (a,b) SEM images of bare microtubes with different magnifications. (c,d) SEM images of the ALD-ZnO−Y_2O_3/ZrO_2 microtube with different magnifications. (e,f) SEM images of PF-MC with different magnifications. The inset in (f) shows the enlarged image. (g) Cross-sectional TEM image of PF-MC. (h) Enlarged cross-sectional TEM image of the "MOF−tube−MOF" structure. (i) Elemental mapping results of the cross section of PF-MC.

obvious morphology change can be noted, demonstrating the conformality and the uniformity of the ALD coating. While an obvious color change can be observed in the optical microscopy image due to the change in the light interference after the addition of the ZnO nanomembrane (Figures S1 and S2). The PF-MC was finally obtained after a gaseous conversion reaction in the nitrogen atmosphere, where the ZnO nanomembrane was transformed into the target ZIF-8 film. During this gaseous conversion process, Zn^{2+} in the ALD ZnO was coordinated with 2-MI vapor continuously, leading to the formation of a dense and uniform ZIF-8 layer.[56] The morphologies of obtained PF-MC with different magnifications are shown in Figures 2e,f, and S3. The inset in Figure 2f shows the enlarged image of the PF-MC surface, where a regular shape of dodecahedra with an average particle size of ∼100 nm can be clearly observed, indicating the formation of ZIF-8. It is worth noting that the particle size of ZIF-8 is smaller than that prepared by the traditional wet-chemistry method. This might be ascribed to the thermal shrinkage during the conversion process. Previously, Huo et al.[57] systematically studied the thermally dependent shrinkage phenomenon in many MOFs and meticulously unraveled the underlying mechanism. We believe that a similar process should exist in our experiment, and the small particle size actually helps in forming a dense and uniform ZIF-8 layer, beneficial to the integration of the MOF and the WGM microcavity. The corresponding elemental characterization is shown in Figure S4, which demonstrates the existence of C and N from the surface ZIF-8 film. It is worth noting that the complete gaseous reaction process here is beneficial to the intactness of microtubular geometry (Figures 2e and S3) because the surface tension of the liquid in the wet-chemistry approach may damage the microtube with a subwavelength tube wall. The experimental results here demonstrate that the current surface modification method is mild, uniform, and conformal, and is quite suitable for 3D complex structures.

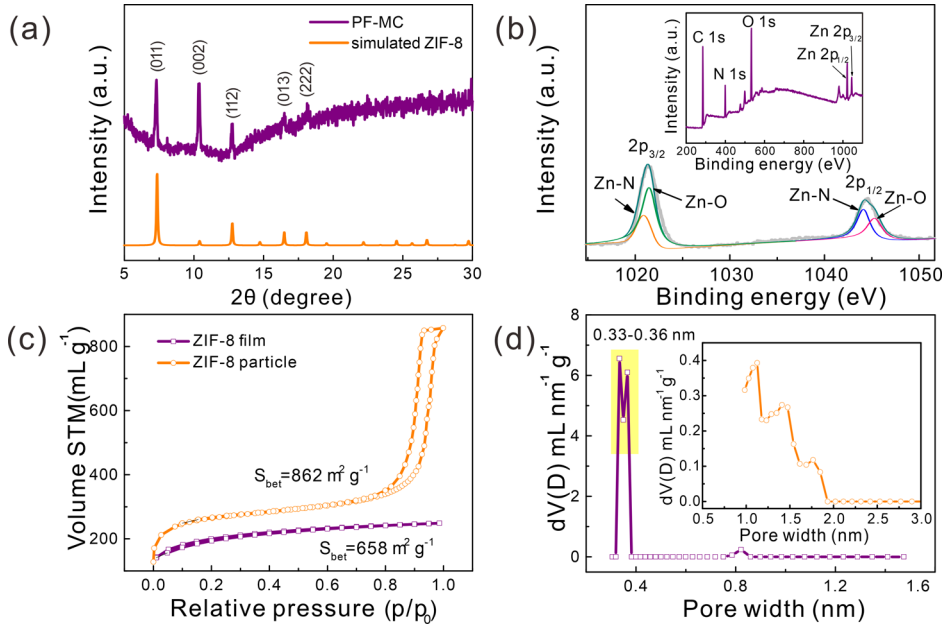

Figure 3. Structural characterization of PF-MC. (a) XRD pattern of the PF-MC and the simulated result. (b) High-resolution Zn 2p XPS spectrum. The inset shows the XPS survey scan. (c) Nitrogen adsorption−desorption isotherms of ZIF-8 films and ZIF-8 particles. (d) Corresponding pore size distributions of ZIF-8 films. The inset shows the pore size distributions of the ZIF-8 particles.

https://doi.org/10.1021/acsami.1c16322
ACS Appl. Mater. Interfaces 2021, 13, 58104−58113

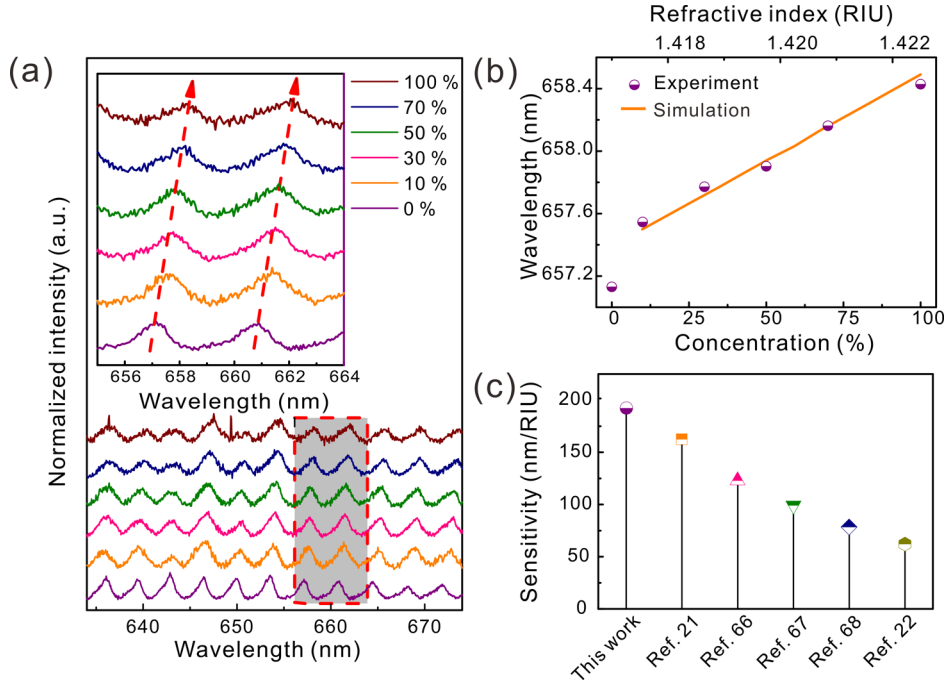

Figure 4. Shift of the resonant wavelength after CO_2 adsorption. (a) Light emission spectra from the PF-MC in the testing chamber filled with a CO_2/N_2 mixture with different CO_2 concentrations. The inset shows the enlarged part corresponding to the red dashed box. (b) Sensing performance of the PF-MC. The purple semi-solid circles are from the experimental results shown in (a). The orange line is plotted according to the simulation. (c) Chart of performances compared with previous literature.

In order to further characterize the composite structure, TEM images of the PF-MC composites are also provided for a closer observation. Focused ion beam was conducted to process the sample for cross-sectional characterization. As shown in Figure 2g, the cross-sectional view of the "MOF−tube−MOF" structure is unraveled. A partial enlargement of the blue dashed box is shown in Figure 2h, and the MOF layer with a thickness of ∼75 nm is noticeable. The TEM image clearly shows the boundary between the ZIF-8 film and the Y_2O_3/ZrO_2 nanomembrane. We ascribe the clear interface between the ZIF-8 film and the tube wall to the gaseous fabrication process with the help of ALD, which is beneficial to light penetration, greatly reducing the scattering loss.[48,49] Figure S5 shows a radial linear scan of the composition along the direction of the blue dashed arrow in Figure 2h. The high N and C concentrations at the side regions originate from the ZIF-8 films which wrap the inside of the Y_2O_3/ZrO_2 nanomembrane with high O concentrations, confirming the unique sandwiched structure. The corresponding elemental mapping of the cross section is shown in Figure 2i. One can see that C, N, O, Al, and Zn elements are evenly distributed on the sample, indicating the uniform growth of ZIF-8 films on the surface of the tube wall. The quantitative elemental analysis (Figure S6) also demonstrates a high mass loading of ZIF-8 films.

We have carried out more characterizations to illuminate the structural and compositional properties of the PF-MC. In order to further investigate the crystal structure of the PF-MC, XRD patterns of the sample are shown in Figure 3a. Sharp peaks of the PF-MC sample located at 2θ = 7.4, 10.4, 12.8, 16.5, and 18° are in good agreement with the simulation based on the crystal structure of ZIF-8 and previous reports[58] and can be correlated to the corresponding crystal planes of (011), (002), (112), (013), and (222), respectively. On the contrary, as shown in Figure S7, the bare microtube and the ALD-ZnO−Y_2O_3/ZrO_2 microtube exhibit a typical broad band from the amorphous structure. Moreover, Raman characterization in Figure S8 further confirms the formation of ZIF-8 films as the peaks from PF-MC should be associated with the 2-MI linker.[59,60] In addition, the elemental composition and chemical states of the composite were investigated by XPS, and the results are shown in Figures 3b and S9. The XPS survey scan in the inset of Figure 3b confirms the presence of C, N, O, and Zn in PF-MC, and more details are obtained from high-resolution spectra. As shown in Figure 3b, the high-resolution Zn 2p spectrum demonstrates two peaks at ∼1021.3 and ∼1044.6 eV, corresponding to Zn $2p_{3/2}$ and Zn $2p_{1/2}$, respectively.[61] The Zn 2p peaks can be further deconvoluted into two sub-peaks corresponding to Zn−O and Zn−N bonds,[61] which is consistent with the ZIF-8 structure. Moreover, Figure S9 exhibits the high-resolution C1s spectrum, and it can be deconvoluted into two sub-peaks, respectively, related to the C/C═C/C−H bond and the C−N/C═N bond in 2-MI.[62] In addition, ESR spectroscopy was used to explore the oxygen vacancies in PF-MC. As shown in Figure S10, the ESR spectrum proves the existence of oxygen vacancies, which create enormous Lewis acid sites and remarkably enhance the gas adsorption ability.[63] The important porous structure of ZIF-8 films was then probed by nitrogen adsorption−desorption isotherms. The results are shown in Figure 3c, and the results from ZIF-8 particles are also demonstrated for comparison. Due to the nanoporous nature of ZIF-8, large specific surface areas are noticeable for both samples. The surface area of 658 $m^2\ g^{-1}$ for ZIF-8 films indicated that the nanoporosity is perfectly retained in the film. We notice that the isotherms of both ZIF-8 particles and films belong to type I isotherms, indicating a typical micropore structure. The corresponding pore size distributions are

https://doi.org/10.1021/acsami.1c16322
ACS Appl. Mater. Interfaces 2021, 13, 58104−58113

Table 1. Typical CO_2 Sensors and Their Sensing Performance

structure	component for gas gathering	linear range	LOD	refs
flat film	polyethylenimine	N. A.	40 ppm	45
flat film	polyethylenimine	390−2000 ppm	390 ppm	46
flat film	polyethylenimine	8−600 ppm	8 ppm	69
flat film	polyethylenimine	0−0.2%	400 ppb	70
flat film	Cu-MOF	N. A.	7×10^{-5} RIU	71
microring	polyhexamethylene biguanide	0−500 ppm	20 ppm	72
microbubble	polyhexamethylene biguanide	200−700 ppm	50 ppm	73
microtube	ZIF-8	10−100%	5.85×10^{-5} RIU	this work

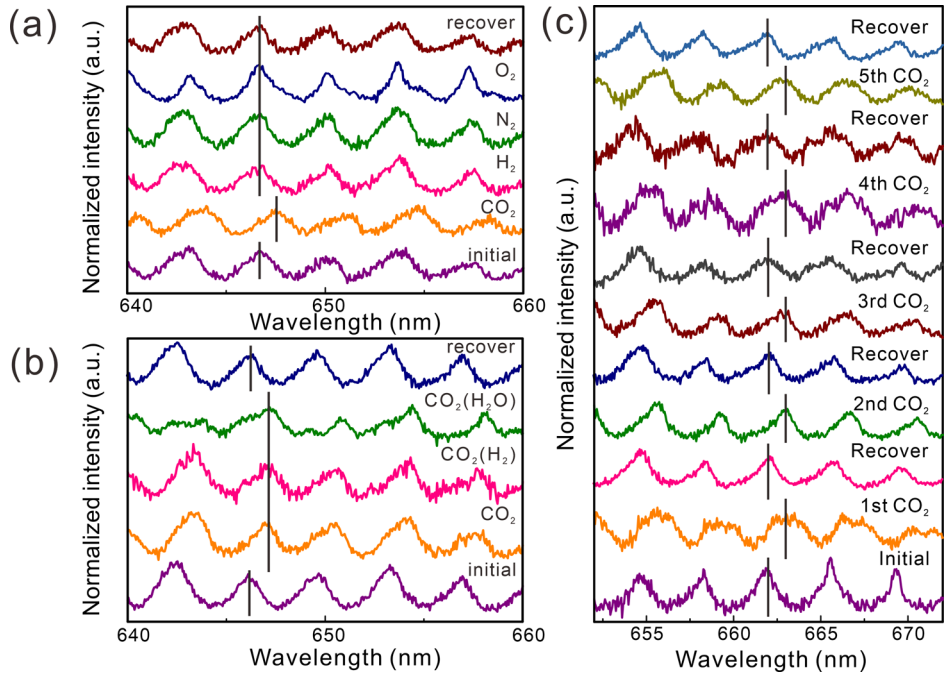

Figure 5. Selectivity and stability performance. (a) Specific adsorption test of the CO_2 sensor. (b) Anti-interference test of the CO_2 sensor. (c) Reproducibility performance of the PF-MC.

demonstrated in Figure 3d and its inset, and a similar microporous structure can be observed in both ZIF-8 particles and ZIF-8 films. Specifically, abundant micropores with the slit width ranging from 0.33 to 0.36 nm exist in the film, confirming the match between the nanoporous ZIF-8 film and the CO_2 gas molecule.[42,43]

3.3. Sensing Performance Evaluation. The obtained PF-MC was used for CO_2 optical sensing, and the collected light emission spectra are illustrated in Figures 4 and S11. In a CO_2 atmosphere, the resonant wavelength exhibits a considerable red shift. This phenomenon is attributed to the RI increase after the ZIF-8 film adsorbs the CO_2 molecules.[20] According to the Lorentz−Lorenz equation, the absorption of CO_2 molecules can increase the density of the ZIF-8 film, resulting in a change in the RI.[20,64] Specifically, as shown in Figure 4a, with the increment of the CO_2 concentration (in N_2) in the testing chamber containing the PF-MC, the resonant wavelength shifts to a longer wavelength gradually. As a control experiment, such a phenomenon cannot be observed in the bare Y_2O_3/ZrO_2 microtubular cavity without the ZIF-8 film when it is immersed in pure CO_2 (Figure S12), indicating that the sensing function is derived from the ZIF-8 film. By further analyzing the shifts of the WGM corresponding to different azimuthal numbers, we observe a slight fluctuation, and the relative standard deviation is calculated to be ∼4.0% (Figure S13), indicating the outstanding system stability of the current PF-MC gas sensor. It is worth noting that the thickness of the MOF layer should also influence the sensing function of the device. Obviously, a thin MOF layer with weak evanescent coupling would lead to a worse performance, which can be reflected by our theoretical simulation. On the contrary, although more adsorbed gas molecules and promoted coupling are beneficial to the sensing performance, we experimentally found that the remarkably increased light scattering make the WGM undetectable. In addition, a too thick MOF film with only the outer part adsorbing gas molecules has a negative effect on evanescent coupling.[65] In our experiment, the MOF layer of ∼75 nm was found to be able to effectively adsorb CO_2 while maintaining a good quality factor simultaneously.

The purple semi-solid circles in Figure 4b show the experimental relationship between the resonant wavelength and the CO_2 concentration, while the orange line in Figure 4b is the simulated relationship between the resonant wavelength and the effective RI. By fitting the experimental results and the simulated results in the linear range (i.e., 10−100%), we can figure out the correspondence between the CO_2 concentration and the RI of the CO_2-absorbed ZIF-8 film. On the basis of the relationship, the sensitivity of the device was also calculated, and a high value of 188 nm RIU^{-1} is obtained (linear regression equation: $Y = 0.007358*X + 661.29$; correlation

https://doi.org/10.1021/acsami.1c16322
ACS Appl. Mater. Interfaces 2021, 13, 58104−58113

coefficient (R^2): 0.99), and the corresponding sensitivity with respect to the CO_2 concentration is 7.4 pm/%. In addition, the LOD is calculated by using the equation LOD = $3\sigma/S$, where σ is the standard deviation and S is the sensitivity. Generally, σ is determined by the line width of the mode and the thermal noise,[31] and it can be estimated as 1/50 of the line width (full width at half maximum of the mode).[33] Thus, a low detection limit of ~5.85×10^{-5} RIU (1.49% in CO_2 concentration) is achieved in the current PF-MC sensor. The detailed comparison of the sensitivity with other optical RI-based gas sensors is summarized in Figure 4c.[21,22,66−68] A more comprehensive comparison of the CO_2 sensing performance of the typical reported sensors and the present work is summarized in Table 1. We should stress that the sensitivity of the PF-MC can compare favorably with plenty of other optical gas sensors in previous reports. The outstanding sensing performance of the current PF-MC can be attributed to the following factors. First, the tubular WGM microcavity with a subwavelength wall thickness is an ideal RI-based sensor due to the intermediate effect of the evanescent field. When the RI of the surrounding medium changes, a corresponding shift of the resonant wavelength will be reflected, which can be employed as the sensing probe. Second, the decoration of surface MOF layers enhances the specific adsorption of CO_2. The gathering of the CO_2 molecules in the neighboring region of the cavity wall causes stronger coupling between the molecules and the evanescent field, and the corresponding RI change makes the composite structure specifically sensitive to detecting CO_2 molecules.

In order to further ensure the selectivity of the PF-MC sensor, its specific adsorption performance was evaluated, and the results are displayed in Figure 5a. Contrary to the sensitive response to CO_2, when the PF-MC is exposed to 4% small-molecule H_2 (in N_2), pure N_2, and pure O_2 (two main components in the air), the obtained spectra exhibit no observable change, confirming the specific sensing ability of CO_2. It should be noted that after being exposed to CO_2, N_2, O_2 and H_2, our gas sensor still exhibits a great recovery property in air (Figure 5a). The anti-interference property is also an important factor to evaluate the sensing performance. We apply pure CO_2 and CO_2 with a small amount (0.01%) of H_2 into the testing chamber and measure the corresponding light emission spectra from the PF-MC. No obvious peak shift with the addition of H_2 can be observed (Figure 5b), indicating an outstanding anti-interference property. The influence of humidity on the stability of the device has also been tested, and ~3% humidity has no obvious influence (Figure 5b).

The underlying mechanism can be explained as follows. With the flow of the CO_2 gas into the test chamber, CO_2 molecules take the place of air due to the specific adsorption originating from the synergistic effect of the pore silt width similar to the dynamic diameter of the CO_2 molecule and the quadrupolar interaction between the carbon atom of the CO_2 molecule and the nitrogen atom of ZIF-8.[41] Consequently, with the RI increase from CO_2 adsorption,[55] a red shift of the resonant wavelength can be observed. When the CO_2 concentration increases, the MOF film tends to adsorb more CO_2 molecules and a continuous red shift was noticed. On the contrary, the H_2 molecule is too small for the pores in the ZIF-8 film, and there is no quadrupolar interaction between H_2 and ZIF-8, so it is easy for H_2 molecules to enter and escape, making ZIF-8 suitable and widely applicable for H_2 separation but not sensing.[74] Other gas molecules, due to a similar reason, are also less selective in terms of size matching and quadrupolar interactions. During the gas-off stage (air atmosphere), the CO_2 molecule desorbs gradually,[20,75] and the RI decreases correspondingly, resulting in the recovery of shifts (Figure 5c). It is worth noting that the desorption time is quite short as less than 1 min (see the experimental results in Figure S14). This indicates the great potential of our device in the fast detection of CO_2 concentration change (mainly limited by the spectrum acquisition time). In addition, the adsorption−desorption process can be repeated many times in our work, and no performance decline can be observed after five cycles (Figure 5c), indicating good reproducibility of the PF-MC. A longer cyclic test was also performed, and the results are demonstrated in Figure S15. The PF-MC device completely recovers after 50 gas-in−gas-out cycles, indicating the outstanding long life cycle ability. It should be noted that, based on the working mechanism mentioned above, this MOF modification approach can be extended to more application scenarios with MOF-decorated WGM microtubular cavities as a sensing platform. The key issue here is to prepare MOF films with specific gas adsorption capability.

4. CONCLUSIONS

In summary, a PF-MC with a sandwiched wall structure was fabricated by combining the rolled-up technology and the gaseous growth process with the ALD ZnO nanomembrane as an induction layer. The resultant PM-FC shows a unique structure, where a homogeneous functional ZIF-8 film is assembled on both the inner and outer surfaces of the Y_2O_3/ZrO_2 microtube. The composite with a nanoporous surface has an ability for selective adsorption of CO_2, and this leads to excellent optical CO_2 sensing in terms of a high sensitivity of 188 nm RIU^{-1} (7.4 pm/% with respect to CO_2 concentration) with a low LOD of ~5.85×10^{-5} RIU. Experimental results also demonstrate that the PF-MC as an optical gas sensor exhibits great selectivity and outstanding reproducibility. This study provides a new strategy to fabricate advanced optical gas sensors and shows great application potential in gas-monitoring-related fields. We believe that the WGM microcavity can be used as a platform to sense different gas molecules once an MOF film with selective gas adsorption ability is prepared by a similar approach. Considering the IC-compatible fabrication of rolled-up microtubes, the current work may have potential for preparing an integrated multiple gas sensing system.

■ ASSOCIATED CONTENT

Supporting Information

The Supporting Information is available free of charge at https://pubs.acs.org/doi/10.1021/acsami.1c16322.

Optical photographs of arrays of Y_2O_3/ZrO_2 microtubes, ALD-ZnO−Y_2O_3/ZrO_2 microtubes, and PF-MCs; SEM image with EDX mapping images of a typical PF-MC, probing the distribution of C, N, O, Al, and Zn; radial linear scan along the dashed arrow in Figure 2h, demonstrating the distribution of the elements in the wall of the PF-MC; elemental concentrations of the PF-MC; XRD patterns of a bare Y_2O_3/ZrO_2 microtube and an ALD-ZnO−Y_2O_3/ZrO_2 microtube; Raman spectrum of the PF-MC compared with those of the bare Y_2O_3/ZrO_2 microtube and the ALD-ZnO−Y_2O_3/ZrO_2 microtube; high-resolution XPS spectra of C 1s; ESR

https://doi.org/10.1021/acsami.1c16322
ACS Appl. Mater. Interfaces 2021, 13, 58104−58113

spectrum of the PF-MC; photoluminescence spectra of the PF-MC and of a bare Y_2O_3/ZrO_2 microtube in the presence and absence of CO_2; shifts of peaks corresponding to resonant modes with different azimuthal numbers; emission spectra of the PF-MC in air and 100% CO_2; and spectra obtained after 5, 10, 20, and 50 gas-in−gas-out cycles (PDF)

AUTHOR INFORMATION

Corresponding Authors

Gaoshan Huang − *Department of Materials Science, Fudan University, Shanghai 200433, P. R. China; International Institute for Intelligent Nanorobots and Nanosystems, Fudan University, Shanghai 200438, P. R. China; Yiwu Research Institute of Fudan University, Yiwu 322000 Zhejiang, P. R. China;* orcid.org/0000-0002-0525-7177; Email: gshuang@fudan.edu.cn

Yongfeng Mei − *Department of Materials Science, Fudan University, Shanghai 200433, P. R. China; International Institute for Intelligent Nanorobots and Nanosystems, Fudan University, Shanghai 200438, P. R. China; Shanghai Frontiers Science Research Base of Intelligent Optoelectronics and Perception, Institute of Optoelectronics, Fudan University, Shanghai 200438, P. R. China; Yiwu Research Institute of Fudan University, Yiwu 322000 Zhejiang, P. R. China;* orcid.org/0000-0002-3314-6108; Email: yfm@fudan.edu.cn

Authors

Ye Kong − *Department of Materials Science, Fudan University, Shanghai 200433, P. R. China; International Institute for Intelligent Nanorobots and Nanosystems, Fudan University, Shanghai 200438, P. R. China*

Zhe Zhao − *Department of Materials Science, Fudan University, Shanghai 200433, P. R. China; International Institute for Intelligent Nanorobots and Nanosystems, Fudan University, Shanghai 200438, P. R. China*

Yunqi Wang − *Department of Materials Science, Fudan University, Shanghai 200433, P. R. China; International Institute for Intelligent Nanorobots and Nanosystems, Fudan University, Shanghai 200438, P. R. China*

Shuo Yang − *Department of Materials Science, Fudan University, Shanghai 200433, P. R. China; International Institute for Intelligent Nanorobots and Nanosystems, Fudan University, Shanghai 200438, P. R. China*

Yang Wang − *Department of Materials Science, Fudan University, Shanghai 200433, P. R. China; International Institute for Intelligent Nanorobots and Nanosystems, Fudan University, Shanghai 200438, P. R. China*

Chang Liu − *Department of Materials Science, Fudan University, Shanghai 200433, P. R. China; International Institute for Intelligent Nanorobots and Nanosystems, Fudan University, Shanghai 200438, P. R. China*

Chunyu You − *Department of Materials Science, Fudan University, Shanghai 200433, P. R. China; International Institute for Intelligent Nanorobots and Nanosystems, Fudan University, Shanghai 200438, P. R. China*

Ji Tan − *State Key Laboratory of High Performance Ceramics and Superfine Microstructure, Shanghai Institute of Ceramics, Chinese Academy of Sciences, Shanghai 200050, P. R. China*

Chao Wang − *Department of Materials Science, Fudan University, Shanghai 200433, P. R. China*

Borui Xu − *Department of Materials Science, Fudan University, Shanghai 200433, P. R. China; Shanghai Frontiers Science Research Base of Intelligent Optoelectronics and Perception, Institute of Optoelectronics, Fudan University, Shanghai 200438, P. R. China; Yiwu Research Institute of Fudan University, Yiwu 322000 Zhejiang, P. R. China;* orcid.org/0000-0001-5357-0400

Jizhai Cui − *Department of Materials Science, Fudan University, Shanghai 200433, P. R. China; International Institute for Intelligent Nanorobots and Nanosystems, Fudan University, Shanghai 200438, P. R. China; Yiwu Research Institute of Fudan University, Yiwu 322000 Zhejiang, P. R. China*

Xuanyong Liu − *State Key Laboratory of High Performance Ceramics and Superfine Microstructure, Shanghai Institute of Ceramics, Chinese Academy of Sciences, Shanghai 200050, P. R. China;* orcid.org/0000-0001-9440-8143

Complete contact information is available at: https://pubs.acs.org/10.1021/acsami.1c16322

Author Contributions

Y.K. and Z.Z. contributed equally to this work. G.H. and Y.M. conceived and supervised the project. Y.K. prepared the samples, performed the sensing experiments, and analyzed the data. Z.Z. helped in analyzing the experimental data and prepared figures. Y.K. and Z.Z. co-wrote the manuscript. Y.W. and Y.W. helped in the theoretical calculation. S.Y. helped in the fabrication and PL test of the sample. J.T. helped in the analyses of XPS. C.L. and C.Y. helped in the morphology characterization. C.W., B.X., J.C, and X.L. helped revise the manuscript. All the authors discussed about the manuscript.

Notes

The authors declare no competing financial interest.

ACKNOWLEDGMENTS

This work was supported by the National Key R&D Program of China (no. 2021YFE0191800), the Natural Science Foundation of China (nos. 51961145108 and 61975035), and the Science and Technology Commission of Shanghai Municipality (nos. 19XD1400600, 20501130700, and 19JC1415500). Part of the experimental work had been carried out in Fudan Nanofabrication Laboratory.

REFERENCES

(1) Fan, W.; Yuan, S.; Wang, W.; Feng, L.; Liu, X.; Zhang, X.; Wang, X.; Kang, Z.; Dai, F.; Yuan, D.; Sun, D.; Zhou, H.-C. Optimizing Multivariate Metal-Organic Frameworks for Efficient C_2H_2/CO_2 Separation. *J. Am. Chem. Soc.* **2020**, *142*, 8728−8737.

(2) Meehl, G. A.; Senior, C. A.; Eyring, V.; Flato, G.; Lamarque, J. F.; Stouffer, R. J.; Taylor, K. E.; Schlund, M. Context for Interpreting Equilibrium Climate Sensitivity and Transient Climate Response from the CMIP6 Earth System Models. *Sci. Adv.* **2020**, *6*, No. eaba1981.

(3) Li, T.; Hasegawa, T.; Yin, X.; Zhu, Y.; Boote, K.; Adam, M.; Bregaglio, S.; Buis, S.; Confalonieri, R.; Fumoto, T.; Gaydon, D.; Marcaida, M.; Nakagawa, H.; Oriol, P.; Ruane, A. C.; Ruget, F.; Singh, B.; Singh, U.; Tang, L.; Tao, F.; Wilkens, P.; Yoshida, H.; Zhang, Z.; Bouman, B. Uncertainties in Predicting Rice Yield by Current Crop Models Under a Wide Range of Climatic Conditions. *Global Change Biol.* **2015**, *21*, 1328−1341.

(4) Brestic, M.; Zivcak, M.; Hauptvogel, P.; Misheva, S.; Kocheva, K.; Yang, X.; Li, X.; Allakhverdiev, S. I. Wheat Plant Selection for High Yields Entailed Improvement of Leaf Anatomical and Biochemical Traits Including Tolerance to Non-Optimal Temperature Conditions. *Photosynth. Res.* **2018**, *136*, 245−255.

(5) Hasanbeigi, A.; Menke, C.; Price, L. The CO_2 Abatement Cost Curve for the Thailand Cement Industry. *J. Clean. Prod.* **2010**, *18*, 1509−1518.
(6) Remiorz, L.; Wiciak, G.; Grzywnowicz, K. Novel Concept of Supporting the Membrane Separation of CO_2 in Power Plants by Thermoacoustic Dehumidification. *Energy* **2019**, *189*, 116191.
(7) Córdoba, P.; Maroto-Valer, M.; Delgado, M. A.; Diego, R.; Font, O.; Querol, X. Speciation, Behaviour, and Fate of Mercury under Oxy-Fuel Combustion Conditions. *Environ. Res.* **2016**, *145*, 154−161.
(8) Engineer, C. B.; Hashimoto-Sugimoto, M.; Negi, J.; Israelsson-Nordström, M.; Azoulay-Shemer, T.; Rappel, W.-J.; Iba, K.; Schroeder, J. I. CO_2 Sensing and CO_2 Peculation of Stomatal Conductance: Advances and Open Questions. *Trends Plant Sci.* **2016**, *21*, 16−30.
(9) Lakhi, K. S.; Park, D.-H.; Al-Bahily, K.; Cha, W.; Viswanathan, B.; Choy, J.-H.; Vinu, A. Mesoporous Carbon Nitrides: Synthesis, Functionalization, and Applications. *Chem. Soc. Rev.* **2017**, *46*, 72−101.
(10) Tan, X.; Zhang, H.; Li, J.; Wan, H.; Guo, Q.; Zhu, H.; Liu, H.; Yi, F. Non-Dispersive Infrared Multi-Gas Sensing via Nanoantenna Integrated Narrowband Detectors. *Nat. Commun.* **2020**, *11*, 5245.
(11) Fine, G. F.; Cavanagh, L. M.; Afonja, A.; Binions, R. Metal Oxide Semi-Conductor Gas Sensors in Environmental Monitoring. *Sensors* **2010**, *10*, 5469−5502.
(12) Korotcenkov, G.; Cho, B. K. Metal Oxide Composites in Conductometric Gas Sensors: Achievements and Challenges. *Sens. Actuators, B* **2017**, *244*, 182−210.
(13) Zhou, H.; Hui, X.; Li, D.; Hu, D.; Chen, X.; He, X.; Gao, L.; Huang, H.; Lee, C.; Mu, X. Metal-Organic Framework-Surface-Enhanced Infrared Absorption Platform Enables Simultaneous On-Chip Sensing of Greenhouse Gases. *Adv. Sci.* **2020**, *7*, 2001173.
(14) Kim, D. Y.; Kang, H.; Choi, N.-J.; Park, K. H.; Lee, H.-K. A Carbon Dioxide Gas Sensor Based on Cobalt Oxide Containing Barium Carbonate. *Sens. Actuators, B* **2017**, *248*, 987−992.
(15) Lin, Y.; Fan, Z. Compositing Strategies to Enhance the Performance of Chemiresistive CO_2 Gas Sensors. *Mater. Sci. Semicond. Process.* **2020**, *107*, 104820.
(16) Marsal, A.; Dezanneau, G.; Cornet, A.; Morante, J. R. A New CO_2 Gas Sensing Material. *Sens. Actuators, B* **2003**, *95*, 266−270.
(17) Jin, Z.; Su, Y.; Duan, Y. Development of A Polyaniline-Based Optical Ammonia Sensor. *Sens. Actuators, B* **2001**, *72*, 75−79.
(18) Kumar, R.; Goel, N.; Kumar, M. UV-Activated MoS_2 Based Fast and Reversible NO_2 Sensor at Room Temperature. *ACS Sens.* **2017**, *2*, 1744−1752.
(19) Paliwal, A.; Sharma, A.; Tomar, M.; Gupta, V. Carbon Monoxide (CO) Optical Gas Sensor Based on ZnO Thin Films. *Sens. Actuators, B* **2017**, *250*, 679−685.
(20) Kim, K.-J.; Lu, P.; Culp, J. T.; Ohodnicki, P. R. Metal-Organic Framework Thin Film Coated Optical Fiber Sensors: A Novel Waveguide-Based Chemical Sensing Platform. *ACS Sens.* **2018**, *3*, 386−394.
(21) Mahros, A. M.; Tharwat, M. M.; Elrashidi, A. Exploring the Impact of Nano-Particles Shape on the Performance of Plasmonic Based Fiber Optics Sensors. *Plasmonics* **2017**, *12*, 563−570.
(22) Vakili, M.; Noori, M. A Highly Accurate Refractive Index Sensor with Two Operation Modes Based on Photonic Crystal Ring Resonator. *Ann. Phys.* **2019**, *531*, 1800453.
(23) Baaske, M. D.; Foreman, M. R.; Vollmer, F. Single-Molecule Nucleic Acid Interactions Monitored on a Label-free Microcavity Biosensor Platform. *Nat. Nanotechnol.* **2014**, *9*, 933−939.
(24) Bavili, N.; Balkan, T.; Morova, B.; Eryürek, M.; Uysalli, Y.; Kaya, S.; Kiraz, A. Highly Sensitive Optical Sensor for Hydrogen Gas Based on a Polymer Microcylinder Ring Resonator. *Sens. Actuators, B* **2020**, *310*, 127806.
(25) Vollmer, F.; Yang, L. Review Label-free detection with high-Q microcavities: a review of biosensing mechanisms for integrated devices. *Nanophotonics* **2012**, *1*, 267−291.
(26) Zhang, J.; Zhong, J.; Fang, Y. F.; Wang, J.; Huang, G. S.; Cui, X. G.; Mei, Y. F. Roll up Polymer/Oxide/Polymer Nanomembranes as a Hybrid Optical Microcavity for Humidity Sensing. *Nanoscale* **2014**, *6*, 13646−13650.
(27) Zhang, S.; Tang, S. J.; Feng, S.; Xiao, Y. F.; Cui, W.; Wang, X.; Sun, W.; Ye, J.; Han, P.; Zhang, X.; Zhang, Y. High-Q Polymer Microcavities Integrated on a Multicore Fiber Facet for Vapor Sensing. *Adv. Opt. Mater.* **2019**, *7*, 1900602.
(28) Huang, G.; Mei, Y. Thinning and Shaping Solid Films into Functional and Integrative Nanomembranes. *Adv. Mater.* **2012**, *24*, 2517−2546.
(29) Wang, Y.; Wang, Y.; Huang, G.; Kong, Y.; Liu, C.; Zhao, Z.; Wu, K.; Mei, Y. Single Whispering Gallery Mode in Mesh-Structured Tubular Microcavity with Tunable Axial Confinement. *Adv. Photonics Res.* **2021**, *2*, 2000163.
(30) Schmidt, O. G.; Eberl, K. Thin solid films roll up into nanotubes. *Nature* **2001**, *410*, 168.
(31) Vahala, K. J. Optical Microcavities. *Nature* **2003**, *424*, 839−846.
(32) Xu, B.; Lin, X.; Mei, Y. Versatile Rolling Origami to Fabricate Functional and Smart Materials. *Cell Rep. Phys. Sci.* **2020**, *1*, 100244.
(33) Huang, G.; Mei, Y. Electromagnetic Wave Propagation in a Rolled-up Tubular Microcavity. *J. Mater. Chem. C* **2017**, *5*, 2758−2770.
(34) Huang, G.; Quiñones, V. A. B.; Ding, F.; Kiravittaya, S.; Mei, Y.; Schmidt, O. G. Rolled-Up Optical Microcavities with Subwavelength Wall Thicknesses for Enhanced Liquid Sensing Applications. *ACS Nano* **2010**, *4*, 3123−3130.
(35) Bavili, N.; Eryürek, M.; Morova, B.; Yilgor, I.; Yilgor, E.; Kiraz, A. Optical Sensors Based on Palladium and Polymer-Coated Optical Fiber Resonators. *Opt. Sens.* **2019**, *11028*, 1102831−1102835.
(36) Zhao, Z.; Zhang, Z.; Zhao, Y.; Liu, J.; Liu, C.; Wang, Z.; Zheng, G.; Huang, G.; Mei, Y. Atomic Layer Deposition Inducing Integration of Co, N Codoped Carbon Sphere on 3D Foam with Hierarchically Porous Structures for Flexible Hydrogen Producing Device. *Adv. Funct. Mater.* **2019**, *29*, 1906365.
(37) James, J. B.; Lang, L.; Meng, L.; Lin, J. Y. S. Postsynthetic Modification of ZIF-8 Membranes via Membrane Surface Ligand Exchange for Light Hydrocarbon Gas Separation Enhancement. *ACS Appl. Mater. Interfaces* **2020**, *12*, 3893−3902.
(38) Meng, F.; Zhang, S.; Ma, L.; Zhang, W.; Li, M.; Wu, T.; Li, H.; Zhang, T.; Lu, X.; Huo, F.; Lu, J. Construction of Hierarchically Porous Nanoparticles@Metal-Organic Frameworks Composites by Inherent Defects for the Enhancement of Catalytic Efficiency. *Adv. Mater.* **2018**, *30*, 1803263.
(39) Denny, M. S.; Moreton, J. C.; Benz, L.; Cohen, S. M. Metal-Organic Frameworks for Membrane-Based Separations. *Nat. Rev. Mater.* **2016**, *1*, 16078.
(40) Chen, X.; Lu, Y.; Dong, J.; Ma, L.; Yi, Z.; Wang, Y.; Wang, L.; Wang, S.; Zhao, Y.; Huang, J.; Liu, Y. Ultrafast In Situ Synthesis of Large-Area Conductive Metal-Organic Frameworks on Substrates for Flexible Chemiresistive Sensing. *ACS Appl. Mater. Interfaces* **2020**, *12*, 57235−57244.
(41) Zhao, Z.; Kong, Y.; Liu, C.; Liu, J.; Wang, Z.; Zheng, G.; Huang, G.; Mei, Y. Atomic Layer Deposition-Induced Integration of N-Doped Carbon Particles on Carbon Foam for Flexible Supercapacitor. *J. Materiomics* **2020**, *6*, 209−215.
(42) Park, K. S.; Ni, Z.; Cote, A. P.; Choi, J. Y.; Huang, R.; Uribe-Romo, F. J.; Chae, H. K.; O'Keeffe, M.; Yaghi, O. M. Exceptional Chemical and Thermal Stability of Zeolitic Imidazolate Frameworks. *Proc. Natl. Acad. Sci. U.S.A.* **2006**, *103*, 10186−10191.
(43) Mottillo, C.; Friščić, T. Carbon Dioxide Sensitivity of Zeolitic Imidazolate Frameworks. *Angew. Chem., Int. Ed.* **2014**, *53*, 7471−7474.
(44) Wang, B.; Côté, A. P.; Furukawa, H.; O'Keeffe, M.; Yaghi, O. M. Colossal Cages in Zeolitic Imidazolate Frameworks as Selective Carbon Dioxide Reservoirs. *Nature* **2008**, *453*, 207−211.
(45) Hasan, D.; Lee, C. Hybrid Metamaterial Absorber Platform for Sensing of CO_2 Gas at Mid-IR. *Adv. Sci.* **2018**, *5*, 1700581.

https://doi.org/10.1021/acsami.1c16322
ACS Appl. Mater. Interfaces 2021, 13, 58104−58113

(46) Bareza, N. J.; Gopalan, K. K.; Alani, R.; Paulillo, B.; Pruneri, V. Mid-infrared Gas Sensing Using Graphene Plasmons Tuned by Reversible Chemical Doping. *ACS Photonics* **2020**, *7*, 879−884.
(47) Zhou, T.; Shen, J.; Wang, Z.; Liu, J.; Hu, R.; Ouyang, L.; Feng, Y.; Liu, H.; Yu, Y.; Zhu, M. Regulating Lithium Nucleation and Deposition via MOF-Derived Co@C-Modified Carbon Cloth for Stable Li Metal Anode. *Adv. Funct. Mater.* **2020**, *30*, 1909159.
(48) Lin, G.; Henriet, R.; Coillet, A.; Jacquot, M.; Furfaro, L.; Cibiel, G.; Larger, L.; Chembo, Y. K. Dependence of Quality Factor on Surface Roughness in Crystalline Whispering-Gallery Mode Resonators. *Opt. Lett.* **2018**, *43*, 495−498.
(49) Wang, N.; Chen, X.; Yang, Y.; Dong, J.; Wang, C.; Yang, G. Diffuse Reflection inside a Hexagonal Nanocavity. *Sci. Rep.* **2013**, *3*, 1298.
(50) Zhao, Z.; Kong, Y.; Lin, X.; Liu, C.; Liu, J.; He, Y.; Yang, L.; Huang, G.; Mei, Y. Oxide Nanomembrane Induced Assembly of A Functional Smart Fiber Composite with Nanoporosity for An Ultra-Sensitive Flexible Glucose Sensor. *J. Mater. Chem. A* **2020**, *8*, 26119−26129.
(51) Zhao, Z.; Kong, Y.; Liu, C.; Huang, G.; Xiao, Z.; Zhu, H.; Bao, Z.; Mei, Y. Atomic Layer Deposition-Assisted Fabrication of 3D Co-Doped Carbon Framework for Sensitive Enzyme-Free Lactic Acid Sensor. *Chem. Eng. J.* **2021**, *417*, 129285.
(52) Li, Y.; Zhao, Y.; Huang, G.; Xu, B.; Wang, B.; Pan, R.; Men, C.; Mei, Y. ZnO Nanomembrane/Expanded Graphite Composite Synthesized by Atomic Layer Deposition as Binder-Free Anode for Lithium Ion Batteries. *ACS Appl. Mater. Interfaces* **2017**, *9*, 38522−38529.
(53) Zhao, Z.; Kong, Y.; Zhang, Z.; Huang, G.; Mei, Y. Atomic Layer-Deposited Nanostructures and Their Applications in Energy Storage and Sensing. *J. Mater. Res.* **2020**, *35*, 701−719.
(54) Lin, X.; Fang, Y.; Zhu, L.; Zhang, J.; Huang, G.; Wang, J.; Mei, Y. Self-Rolling of Oxide Nanomembranes and Resonance Coupling in Tubular Optical Microcavity. *Adv. Opt. Mater.* **2016**, *4*, 936−942.
(55) Cookney, J.; Ogieglo, W.; Hrabanek, P.; Vankelecom, I.; Fila, V.; Benes, N. E. Dynamic Response of Ultrathin Highly Dense ZIF-8 Nanofilms. *Chem. Commun.* **2014**, *50*, 11698−11700.
(56) Stassen, I.; Styles, M.; Grenci, G.; Van Gorp, H.; Vanderlinden, W.; De Feyter, S.; Falcaro, P.; De Vos, D.; Vereecken, P.; Ameloot, R. Chemical Vapour Deposition of Zeolitic Imidazolate Framework Thin Films. *Nat. Mater.* **2016**, *15*, 304−310.
(57) Pan, T.; Shen, Y.; Wu, P.; Gu, Z.; Zheng, B.; Wu, J.; Li, S.; Fu, Y.; Zhang, W.; Huo, F. Thermal Shrinkage Behavior of Metal-Organic Frameworks. *Adv. Funct. Mater.* **2020**, *30*, 2001389.
(58) Yao, J.; Chen, R.; Wang, K.; Wang, H. Direct Synthesis of Zeolitic Imidazolate Framework-8/Chitosan Composites in Chitosan Hydrogels. *Microporous Mesoporous Mater.* **2013**, *165*, 200−204.
(59) Carter, D. A.; Pemberton, J. E. Raman Spectroscopy and Vibrational Assignments of 1- and 2-Methylimidazole. *J. Raman Spectrosc.* **1997**, *28*, 939−946.
(60) Zhao, Z.; Liu, S.; Zhu, J.; Xu, J.; Li, L.; Huang, Z.; Zhang, C.; Liu, T. Hierarchical Nanostructures of Nitrogen-Doped Porous Carbon Polyhedrons Confined in Carbon Nanosheets for High-Performance Supercapacitors. *ACS Appl. Mater. Interfaces* **2018**, *10*, 19871−19880.
(61) Tuncel, D.; Ökte, A. N. Improved Adsorption Capacity and Photoactivity of ZnO-ZIF-8 Nanocomposites. *Catal. Today* **2021**, *361*, 191−197.
(62) Hayashi, M.; Lee, D. T.; de Mello, J. A.; Boscoboinik, J. A.; Tsapatsis, M. ZIF-8 Membrane Permselectivity Modification by Manganese(II) Acetylacetonate Vapor Treatment. *Angew. Chem., Int. Ed.* **2021**, *60*, 9316−9320.
(63) Wen, L.; Li, X.; Zhang, R.; Liang, H.; Zhang, Q.; Su, C.; Zeng, Y.-J. Oxygen Vacancy Engineering of MOF-Derived Zn-Doped Co_3O_4 Nanopolyhedrons for Enhanced Electrochemical Nitrogen Fixation. *ACS Appl. Mater. Interfaces* **2021**, *13*, 14181−14188.
(64) Owens, J. C. Optical Refractive Index of Air: Dependence on Pressure, Temperature and Composition. *Appl. Opt.* **1967**, *6*, 51−59.
(65) Lee, J.; Lee, K.; Kim, J. Fiber-Based Gas Filter Assembled via in situ Synthesis of ZIF-8 Metal Organic Frameworks for An Optimal Adsorption of SO_2: Experimental and Theoretical Approaches. *ACS Appl. Mater. Interfaces* **2021**, *13*, 1620−1631.
(66) Chen, W. P.; Wang, D. N.; Xu, B.; Wang, Z. K.; Zhao, C.-L. Fabry-Perot Interferometer Fiber Tip Sensor Based on A Glass Microsphere Glued at the Etched End of Multimode Fiber. *Opt. Eng.* **2017**, *56*, 057107.
(67) Sun, S.; Xu, Y.; Ren, L.; Xu, J.; Jia, T.; Zhang, L.; Xiao, J.; Wang, B.; Yang, W.; Cheng, S.; Chen, F.; Ma, C.; Song, F. Research on the Gas Refractive Index Sensing Based on Microfiber Double-Knot Resonator with a Parallel Structure. *Optik* **2020**, *204*, 164207.
(68) González-Vila, Á.; Ioannou, A.; Loyez, M.; Debliquy, M.; Lahem, D.; Caucheteur, C. Surface Plasmon Resonance Sensing in Gaseous Media with Optical Fiber Gratings. *Opt. Lett.* **2018**, *43*, 2308−2311.
(69) Zhou, Y.; Wang, Y.; Wang, Y.; Li, X. Humidity-Enabled Ionic Conductive Trace Carbon Dioxide Sensing of Nitrogen-Doped $Ti_3C_2T_x$ MXene/Polyethyleneimine Composite Films Decorated with Reduced Graphene Oxide Nanosheets. *Anal. Chem.* **2020**, *92*, 16033−16042.
(70) Pohl, T.; Sterl, F.; Strohfeldt, N.; Giessen, H. Optical Carbon Dioxide Detection in the Visible Down to the Single Digit ppm Range Using Plasmonic Perfect Absorbers. *ACS Sens.* **2020**, *5*, 2628−2635.
(71) Kreno, L. E.; Hupp, J. T.; Van Duyne, R. P. Metal−Organic Framework Thin Film for Enhanced Localized Surface Plasmon Resonance Gas Sensing. *Anal. Chem.* **2010**, *82*, 8042−8046.
(72) Mi, G.; Horvath, C.; Aktary, M.; Van, V. Silicon microring refractometric sensor for atmospheric CO_2 gas monitoring. *Opt. Express* **2016**, *24*, 1773−1780.
(73) Li, H.; Sun, B.; Yuan, Y.; Yang, J. Guanidine derivative polymer coated microbubble resonator for high sensitivity detection of CO2 gas concentration. *Opt. Express* **2019**, *27*, 1991−2000.
(74) Etxeberria-Benavides, M.; Johnson, T.; Cao, S.; Zornoza, B.; Coronas, J.; Sanchez-Lainez, J.; Sabetghadam, A.; Liu, X.; Andres-Garcia, E.; Kapteijn, F.; Gascon, J.; David, O. PBI Mixed Matrix Hollow Fiber Membrane: Influence of ZIF-8 Filler over H_2/CO_2 Separation Performance at High Temperature and Pressure. *Sep. Purif. Technol.* **2020**, *237*, 116347.
(75) Tian, H.; Fan, H.; Li, M.; Ma, L. Zeolitic Imidazolate Framework Coated ZnO Nanorods as Molecular Sieving to Improve Selectivity of Formaldehyde Gas Sensor. *ACS Sens.* **2016**, *1*, 243−250.

https://doi.org/10.1021/acsami.1c16322
ACS Appl. Mater. Interfaces 2021, 13, 58104−58113